Tower testing of a 64W shortwave infrared supercontinuum laser for use as a hyperspectral imaging illuminator

Joseph Meola[a], Anthony Absi[a], Mohammed N. Islam[b], Lauren M. Peterson[b], Kevin Ke[b], Michael J. Freeman[b], Agustin I. Ifaraguerri[c]

[a]Air Force Research Laboratory, WPAFB, OH 45433
[b] Omni Sciences, Inc., Dexter, MI 48105
[c] Leidos, Inc., Arlington, VA 22203

ABSTRACT

Hyperspectral imaging systems are currently used for numerous activities related to spectral identification of materials. These passive imaging systems rely on naturally reflected/emitted radiation as the source of the signal. Thermal infrared systems measure radiation emitted from objects in the scene. As such, they can operate at both day and night. However, visible through shortwave infrared systems measure solar illumination reflected from objects. As a result, their use is limited to daytime applications. Omni Sciences has produced high powered broadband shortwave infrared super-continuum laser illuminators. A 64-watt breadboard system was recently packaged and tested at Wright-Patterson Air Force Base to gauge beam quality and to serve as a proof-of-concept for potential use as an illuminator for a hyperspectral receiver. The laser illuminator was placed in a tower and directed along a 1.4km slant path to various target materials with reflected radiation measured with both a broadband camera and a hyperspectral imaging system to gauge performance.

Keywords: hyperspectral, supercontinuum, active, shortwave infrared

1. INTRODUCTION

Use of hyperspectral imaging (HSI) systems continues to grow due to their ability to passively collect spectral characteristics of materials from long ranges.[1] These spectral characteristics are then used to perform various exploitation tasks, such as material identification[2] and target detection.[3,4] Shortwave infrared (SWIR) HSI systems typically operate in the 1.0-2.5μm waveband. As such, SWIR systems typically measure solar illumination reflected from scene objects. As a result, the operability of current SWIR systems is limited to conditions with adequate solar illumination, which precludes operation at night and low solar illumination levels (dawn, evening, overcast). While thermal HSI systems possess day/night operability, the sensor and detector technology is not as mature as those operating in the reflective region. SWIR HSI systems typically offer superior spatial and spectral resolution with lower noise when compared with thermal systems.[5] Additionally, key spectral identification features of various materials exist in the SWIR waveband. Development of a SWIR HSI system coupled with an on-board light source would allow for improved operability for such exploitation tasks.

Broadband, high power lamps exist as potential on-board light sources for reflective HSI systems. However, these sources are difficult to collimate and direct with small divergence over long distances. Conventional lasers with high brightness and low divergence are available, but their narrow spectral bandwidth limits their utility as an illumination source for HSI systems. While multi-spectral systems have been developed using multiple narrowband laser sources,[6] extension to hyperspectral systems would be impractical. Super-continuum lasers (SCLs) share with conventional lasers useful characteristics such as high brightness and low divergence. However, unlike conventional lasers, SCLs possess a broad spectral bandwidth.[7] Additionally, the spectral power density of the SCL can be engineered to produce sources with power over a predefined wavelength range, providing improved energy efficiency when compared to lamp sources. With the advent and continued development of high-powered SCLs, these sources provide a candidate for use in developing an "active HSI" system. A number of challenges exist with the use of SC lasers as illumination sources. Modeling of the radiative transfer process and calibration associated with the system is complicated by the spectral dependence of laser divergence properties. Additionally, atmospheric turbulence effects must be mitigated. Recent work using a visible to near infrared SCL

Algorithms and Technologies for Multispectral, Hyperspectral, and Ultraspectral Imagery XX, edited by Miguel Velez-Reyes, Fred A. Kruse, Proc. of SPIE Vol. 9088, 90881A · © 2014 SPIE · CCC code: 0277-786X/14/$18 · doi: 10.1117/12.2056722

has demonstrated potential as an illumination source and has also illustrated several of the challenges mentioned here.[8]

The AFRL, Omni Sciences, Inc.,[9] and Leidos, Inc. have coordinated in the development and testing of SSCL sources for HSI illumination. Previous tower testing was performed using a 5W SWIR SCL (SSCL) prototype operating from $1.5 - 2.4\mu m$ with a broadand SWIR camera and a SWIR point-sample field spectrometer.[10–12] This initial testing demonstrated the robust opeartion of the SSCL and the ability to retrieve spectral reflectance of materials using the SSCL as the sole source of illumination. Further SSCL development has resulted in a 64W breadboard SSCL operating over a spectral range of $1.0 - 1.8\mu$m. A repeat tower trial was performed at Wright Patterson Air Force Base (WPAFB) in November 2013 to assess the SSCL characteristics (beam divergence, beam quality, spectral power density). In addition to the SWIR broadband camera and the point spectrometer, a slit-based SWIR imaging spectrometer was incorporated into the test to gauge the challenges associated with generating hyperspectral image cubes using a SSCL light source. In Section 2, a brief discussion of the SSCL is given. In Section 3, an updated radiometric system model is provided. In Section 4, the tower test experiments are outlined in detail and the results discussed. Finally, in Section 5, a summary is provided along with discussion of on-going and future work in this area.

2. SUPERCONTINUUM LASER

Omni Sciences, Inc. has developed a 64W SWIR SCL operating from 1.064μm to greater than 1.8μm assembled entirely from commercial off-the-shelf (COTS) fiber optical components from the fiber communications industry.

2.1 Laser development

Figure 1 shows the block diagram for the 64W SCL, which is essentially a MOPA (master oscillator-power amplifier). The laser diode provides the seed radiation at 1.064μm for the Yb-doped polarization-maintaining fiber (5m long) preamplifier, which is a diode laser pumped through its cladding with up to 8 W at 0.922μm. The amplified radiation is filtered and sent to the cladding-pumped fiber mid-amplifier (3 m long) followed by the power amplifier (22 m long) for further amplification. These amplifiers are also cladding-pumped by laser diodes with up to 10 W and 180 W, respectively, at 0.915μm. The seed laser is operated with a pulse duration of 0.45 nsec with a variable repetition rate set using computer-controlled drive electronics. Typical operation is between 1 MHz to 20 MHz. The high average power and high peak power (up to 20 KW) pulses of the amplified radiation propagate through 10 m of un-doped fused silica fiber (25/400; NA = 0.065), where the supercontinuum is generated. Since the 1.064μm radiation is well below the zero dispersion wavelength of 1.3μm for the silica fiber, Stokes stimulated Raman scattering in the fiber serves to shift the wavelength to beyond 1.3μm in multiple steps. Beyond the zero dispersion wavelength, nonlinear optical processes that include modulation instability, optical mixing, and self-phase modulation lead to the generation of the broad continuum out to about 2μm. Figure 2 presents a picture of the laser with the fiber delivery cable to the optical collimator along with the laptop controller. Further information on the SCL technology can be found in the authors' references.

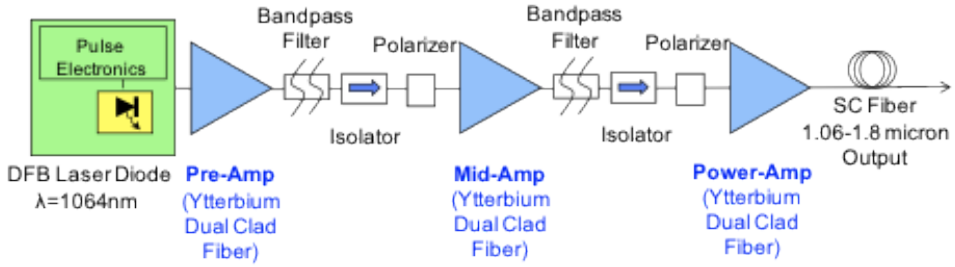

Figure 1: Block diagram for 64W SWIR supercontinuum laser

Figure 2: 64W SWIR supercontinuum laser

2.2 Laboratory characterization

The output power of the SSCL was measured in the lab at WPAFB just prior to the tower test. The total integrated power of the laser was measured around 64W using a thermal power meter. The spectral power density was measured using a field spectrometer with the laser illumination reflected from a diffuse, spectrally uniform material (Spectralon). The spectrometer measurements were corrected to account for the spot sample to provide an accurate measure of the spectral power density. Figure 3 displays the measured spectral power density for the 64W laser source. The spectral power density demonstrates significant residual pump laser

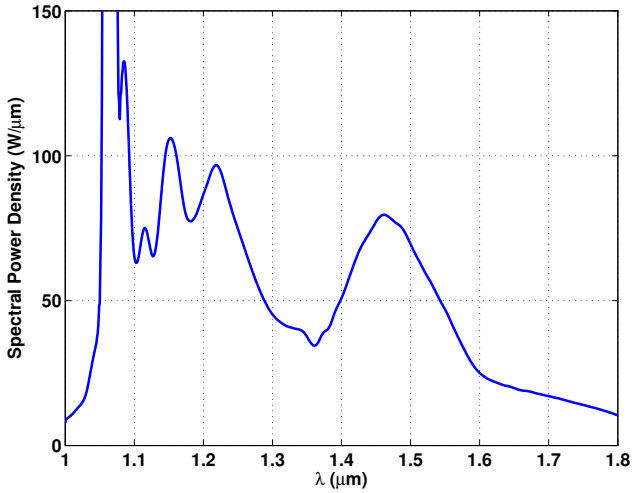

Figure 3: 64W SWIR supercontinuum laser spectral power density

power around 1.06μm with relatively uniform power distribution over 1.1-1.6μm. The full-angle laser beam divergence θ is measured to be approximately 0.636mrad at 1.4μm. Measurements were additionally collected to demonstrate the progression of the supercontinuum process. For these measurements, the diode laser pump power was increased linearly from 8 W to 165 W. As the pump power is increased, the peak power from the power amplifier is also increased. This leads to a greater proliferation of nonlinear effects in the SC fiber, which leads to laser broadening to longer wavelengths. These results are observed in Figure 4.

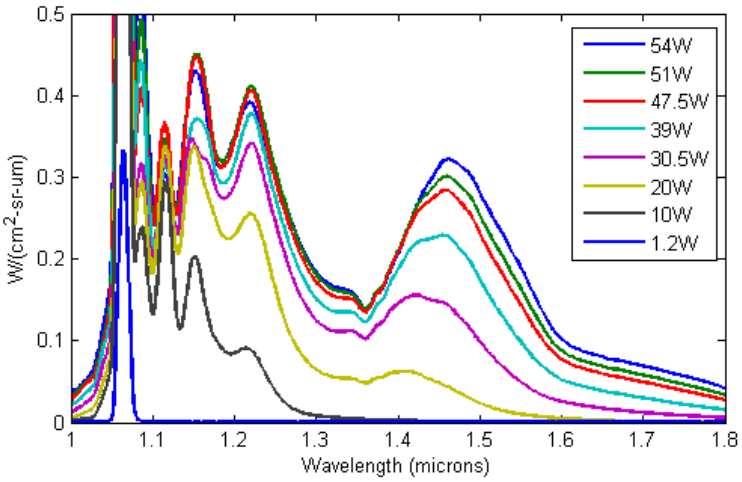

Figure 4: Progression of the supercontinuum with increased power

3. RADIOMETRIC MODELING

A radiometric model was previously developed to understand the relationship between laser propagation and measured radiation.[12] The model is revisited and adapted here to reflect properties of a slit-based hyperspectral imaging system. A SWIR HSI system was used for the field test to measure propagated beam characteristics as a function of wavelength. The camera operates over a wavelength range of 1-2.5μm, which sufficiently covers the spectral range of the SSCL. A simplified model describing the spectral radiance reaching the HSI sensor aperture at nighttime is given by,

$$L_p(\lambda) = \frac{E(\lambda)}{\pi}\tau^2(\lambda)\rho(\lambda) + L_{BS}(\lambda) \tag{1}$$

where E is the spectral irradiance of the laser on the target surface (with no atmospheric loss), ρ is the target spectral reflectance, τ is the atmospheric transmission along the laser-to-target path, and L_{BS} is laser backscatter that may exist.

Using the detector irradiance, one can estimate the number of photoelectrons detected from the signal and background. For this analysis, the signal is considered the portion of the pupil-plane radiance comprised of radiance reflected by the target material. The background is considered the entire pupil-plane radiance, which would include any laser backscatter that may exist. The photon arrival/detection is a random process, therefore, the number of detected photoelectrons for the signal, N_s and for the background N_b are both random processes. The mean detected photoelectrons for the signal and background for integration time t_d is estimated by,

$$\begin{aligned} \mu_s &= A_d t_d \frac{\min(M_{spec}s, w)}{w} \int \frac{\lambda}{hc}\eta(\lambda)E_s(\lambda)d\lambda \\ \mu_b &= A_d t_d \frac{\min(M_{spec}s, w)}{w} \int \frac{\lambda}{hc}\eta(\lambda)E_b(\lambda)d\lambda \end{aligned} \tag{2}$$

where A_d is the detector area, η is the detector quantum efficiency, s is the slit width, M_{spec} is the spectrometer magnification, and w is the detector width. Additionally, E_s and E_b represent the signal and background spectral irradiance incident on the detector. Typically, the magnified slit and detector size are matched, which would remove the fraction term from the equation. Assuming the spectral bandwidth $\delta\lambda_k$ of the sensor is small, the integrated photons for a particular band k can be approximated by,

$$\begin{aligned} \mu_s[\lambda_k] &= A_d t_d \frac{\min(M_{spec}s, w)}{w} \frac{\lambda_k}{hc}\eta(\lambda_k)E_s(\lambda_k)\delta\lambda_k \\ \mu_b[\lambda_k] &= A_d t_d \frac{\min(M_{spec}s, w)}{w} \frac{\lambda_k}{hc}\eta(\lambda_k)E_b(\lambda_k)\delta\lambda_k \end{aligned} \tag{3}$$

Using these definitions for signal and background, the SNR for a given band is,

$$SNR[\lambda_k] = \frac{\mu_s[\lambda_k]}{\sqrt{\mu_b[\lambda_k] + \mu_d + \sigma^2_{read}}} \tag{4}$$

where μ_d is the mean number of dark photoelectrons and σ_{read} is the electronic read noise. This model fails to incorporate the impact of atmospheric turbulence. The pupil-plane radiance will have increased temporal variability due to turbulence. The exact model for this increased variance is unclear at this time, but is added as an additional noise term, σ_{turb}, which is assumed to have a spectral dependence. The final SNR is then given by,

$$SNR[\lambda_k] = \frac{\mu_s[\lambda_k]}{\sqrt{\mu_b[\lambda_k] + \mu_d + \sigma^2_{read} + \sigma^2_{turb}[\lambda_k]}} \tag{5}$$

4. TOWER TESTING

Tower-based testing of the 64W SSCL was performed to assess beam propagation characteristics of the laser and to demonstrate reflectance retrieval capabilities. The tower test and resulting analysis are presented here.

4.1 Test overview

The tower test occurred at WPAFB from 4-7 November 2013. The majority of testing occurred after sunset to remove any solar contribution to the measured signal. For these tests, the SSCL was placed in a tower and directed along a slant path to a target panel on the ground. Figure 5 provides a sideview diagram of the tower-based test setup. The target panel consists of a plywood stand for placement/holding of the target materials

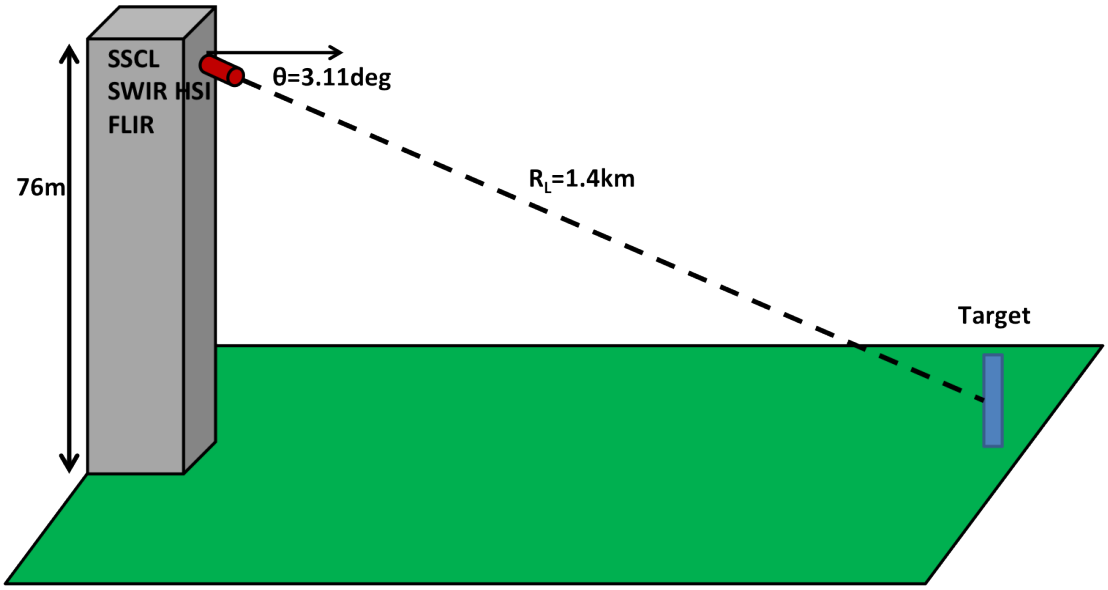

Figure 5: Diagram of tower-based test

used during the collection. The materials used include Tyvek, black silt cloth, gray silt cloth, a blue tarp, and gray painted plywood. The stand is tilted slightly to create a normal surface with respect to the laser beam propagation angle (3.11°). In this diagram, the laser range R_L is determined by the slant range from the tower (1.4km). A broadband SWIR camera was utilized to provide beam shape and turbulence analysis. Additionally, a slit-based SWIR HSI system was used to measure the spectral characteristics of the laser as a function of wavelength. Both the broadband and HSI cameras were equipped with 100mm lenses to provide multiple pixels across the 0.9m laser spot diameter at a 1.4km slant range. Other relevant laser and camera specifications for the tower test are provided in Table 1. Note that due to losses in the mirrors used to direct the laser beam from the tower, the effective laser power is approximately 55W rather than the lab measured 64W.

R_L(km)	1.4
Output Power (W)	55
Full-angle divergence @ 1.4um (mrad)	0.636
Spot size @ 1.4um (m)	0.9
IFOV (mrad)	0.3
GSD (cm)	42

Table 1: Relevant specifications for tower test

4.2 Beam shape

The broadband camera was placed both in the field near the plywood target stand to collect high spatial resolution imagery of the beam and in the tower to demonstrate adequate SCL signal level for collection at longer ranges. Figure 6 displays both the high resolution field image and the tower image. The images demonstrate a somewhat

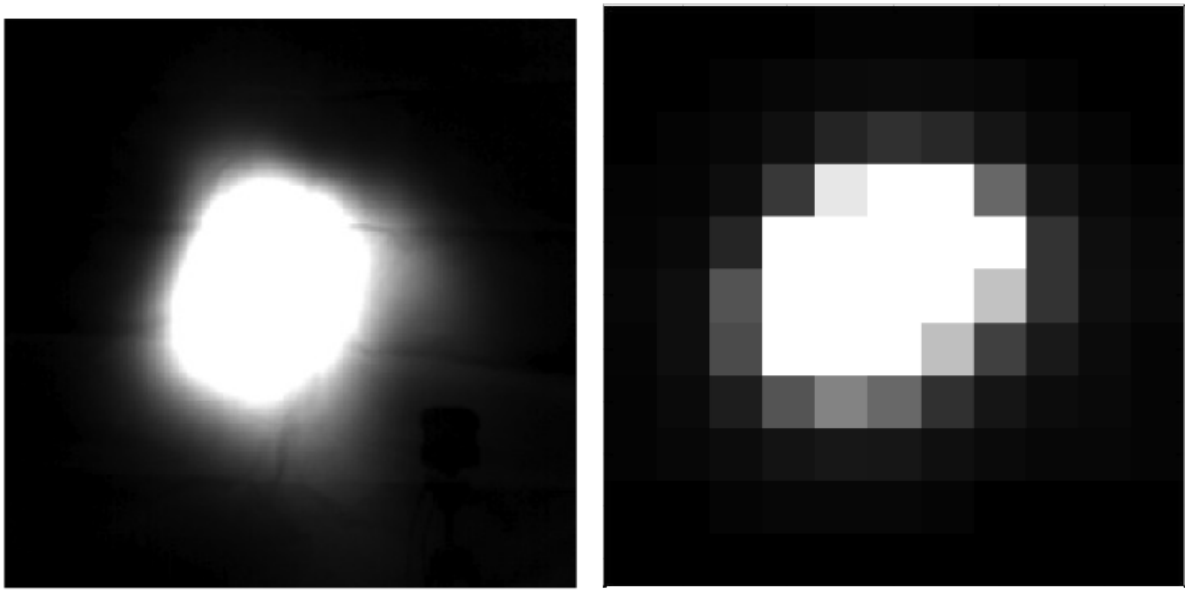

(a) Field **(b) Tower**

Figure 6: Broadband images of laser spot as collected from (a) the field and (b) the tower.

elliptical laser spot that is rotated slightly clockwise. This slight beam deformation is attributed to heating of the optical elements used to direct the beam to the target. As an additional test of the laser beam quality as related to wavelength, the laser was directed towards the uniform Spectralon target in the lab. The HSI camera then collected spectral imagery of the center portion of the beam. Being a slit-based imaging spectrometer, this imagery provides a center beam profile as a function of wavelength. Figure 7 displays the beam profile for a subset of spectral bands across the spectral range of the laser. The beam profile is not perfectly Gaussian, which again may be attributed to imperfect optics used to direct the beam.

4.3 Radiometric analysis

In addition to beam shape analysis, the spectral SNR is estimated for a number of target materials. In order to estimate the mean pupil-plane radiance for a given target material, 1000 hyperspectral images are collected for each target. The collection of such a large number of data cubes was made possible by the fact that the laser spot occupies only a few spatial pixels on the target at a range of 1.4km. A calibrated light source was used to radiometrically correct the data for conversion from digital numbers to physical radiance units. The temporal mean provides an estimate of the mean pupil-plane radiance, while the temporal standard deviation provides information on both turbulence effects and sensor noise. The beam spot is expected to occupy an area of approximately 2x2 pixels in the imagery. The mean and standard deviation are averaged in the brightest 2x2 area for

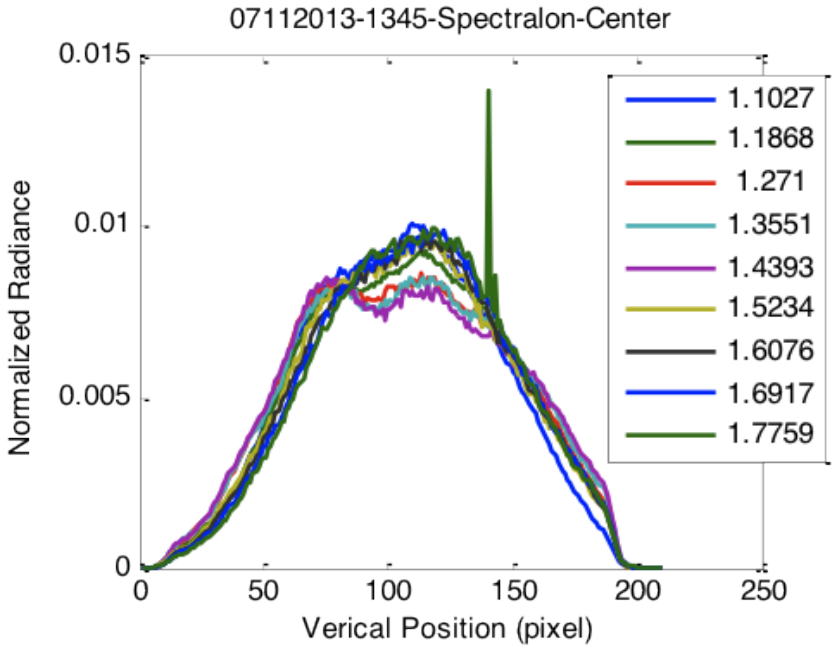

Figure 7: Beam profile as a function of wavelength

each set of data cubes collected to be representative of the average within the laser spot. Figure 8 displays the spectral mean and standard deviation for different target materials. It is noted that the camera integration time was optimized for each material to utilize most of the camera dynamic range, but was generally between 1-5ms. In general, the standard deviation possesses the same spectral shape as the mean signal suggesting that shot

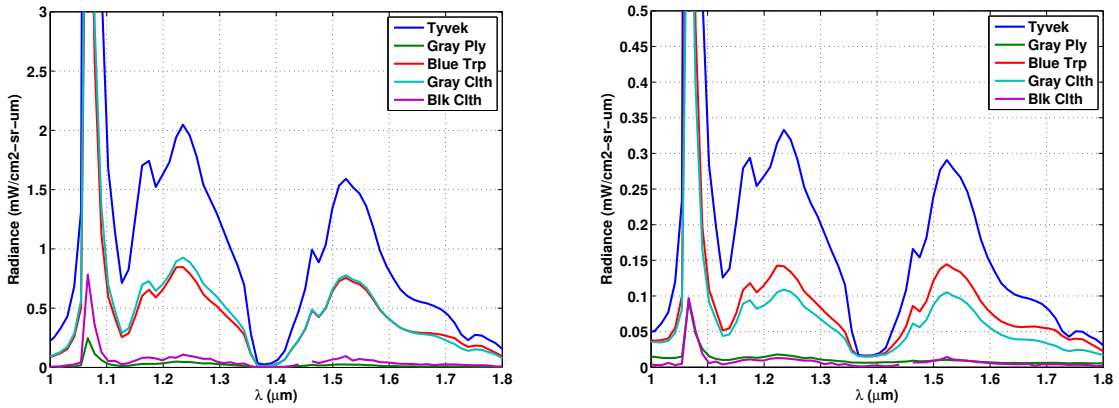

(a) Sample mean **(b) Sample standard deviation**

Figure 8: Mean and standard deviation of spectral radiance at sensor aperture for different target materials

noise and turbulence are the predominant noise sources. Figure 9 displays the estimated SNR for each target material as the ratio of the mean and standard deviation. Further radiometric analysis is performed using the Tyvek target. The predicted sensor-reaching radiance is computed using the measured spectral power density output of the laser obtained using the field spectrometer in the lab as shown in Figure 3. The laser output is used with modeled atmospheric transmission obtained using MODTRAN[13,14] with radiosonde data collected on the evening of 5 November and with laboratory "reflectance truth" for Tyvek. Figure 10 displays the modeled atmospheric transmission. Figure 11 displays a comparison of the modeled and measured pupil-plane radiance

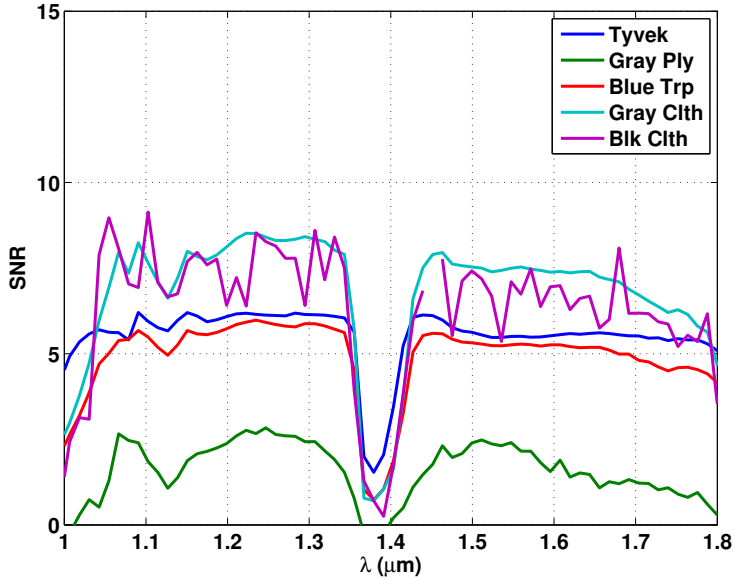

Figure 9: SNR for different target materials

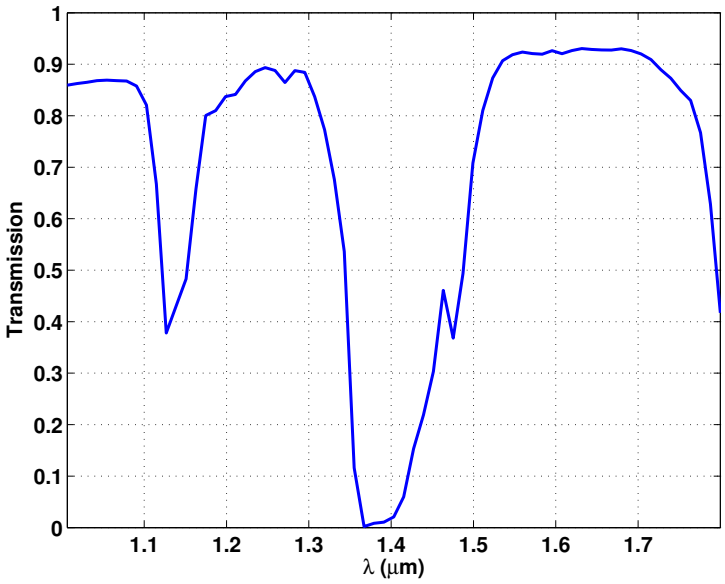

Figure 10: Modeled atmospheric transmission obtained from MODTRAN using sonde data

for Tyvek along with a predicted SNR. The predicted SNR is obtained using the model outlined above with realistic estimates for the unknown noise and spectrometer parameters. The turbulence effect is ignored in the model at this point. The predicted SNR for Tyvek is much larger than the actual measured SNR shown in Figure 9. The measured SNR is relatively flat spectrally suggesting that performance is limited by turbulence rather than signal level.

For further insight into the variability of the sensor-reaching radiance, a temporal analysis of the peak spot for the Tyvek material is examined. Figure 12 displays a subset of the temporal hyperspectral samples collected for the Tyvek material at the brighest pixel. The figure additionally shows a histogram of the mean-subtracted

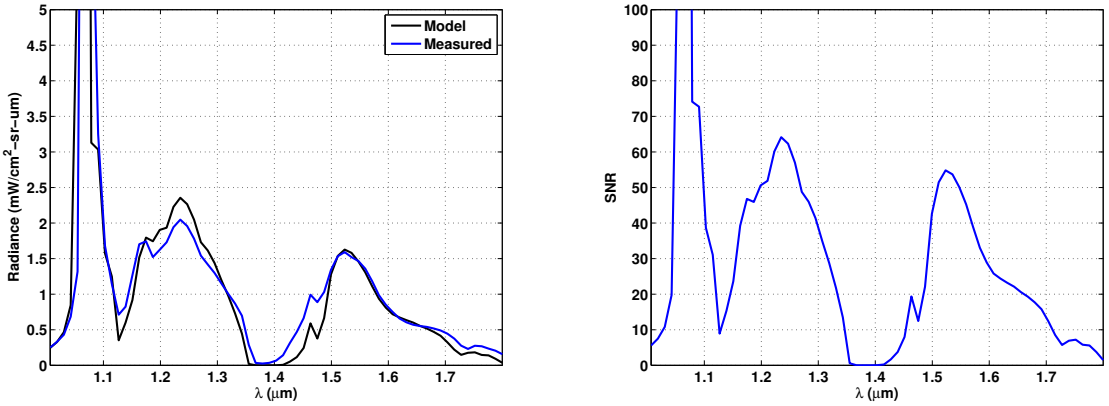

(a) Model and measured radiance comparison **(b) Modeled SNR**

Figure 11: Model results for Tyvek

temporal data at a band near 1.2μm. The shape of the histogram is skewed. A quick literature search shows

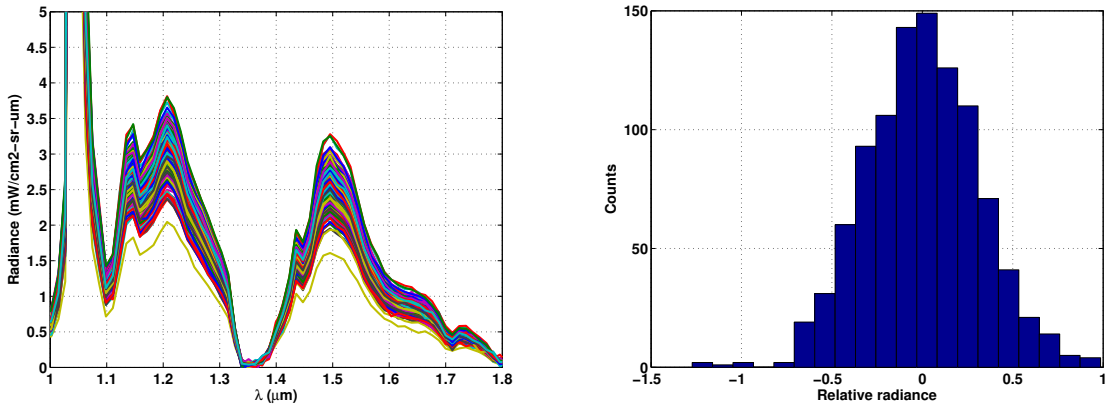

(a) Temporal samples **(b) Histogram of mean-subtracted temporal samples at 1.2μm**

Figure 12: Variance analysis for peak spot of measured Tyvek radiance

that scintillation effects are sometimes modeled using a log-normal distribution function, which is right-skewed as the data here appears to be.[15] These results further suggest that performance is limited by turbulence.

4.4 Reflectance retrieval

An emprical line method (ELM) technique is employed to retrieve spectral reflectance of the targets from the HSI. The sensor-reaching radiance given in (1), can be written as a linear function of material reflectance,

$$L_p(\lambda_k) = a(\lambda_k)\rho(\lambda_k) + b(\lambda_k) \tag{6}$$

where

$$\begin{aligned} a(\lambda_k) &= \frac{E(\lambda_k)}{\pi}\tau^2(\lambda_k) \\ b(\lambda_k) &= L_{BS}(\lambda_k) \end{aligned} \tag{7}$$

For the ELM, $\hat{a}$ and $\hat{b}$ are estimated in-scene using materials with known reflectances. Typically, two known materials are used to obtain the estimates,

$$\hat{a}(\lambda_k) = [L_1(\lambda_k) - L_2(\lambda_k)]/[\rho_1(\lambda_k) - \rho_2(\lambda_k)] \tag{8}$$

and

$$\hat{b}(\lambda_k) = [L_2(\lambda_k)\rho_1(\lambda_k) - L_1(\lambda_k)\rho_2(\lambda_k)]/[\rho_1(\lambda_k) - \rho_2(\lambda_k)] \quad (9)$$

where ρ_1 and ρ_2 are the known reflectances of the two materials and L_1 and L_2 are the in-scene measurements associated with these same two materials. For the analysis performed here, the gray silt cloth and black silt cloth targets are used as the two known materials.

Using $\hat{a}$ and $\hat{b}$ computed from the black and gray silt cloth material, the spectral reflectances of the Tyvek and blue tarp materials are estimated from the mean spectral radiance of these materials given in Figure 8. Figure 13 displays the retrieved reflectance using ELM. The retrieved reflectance for the Tyvek material demon-

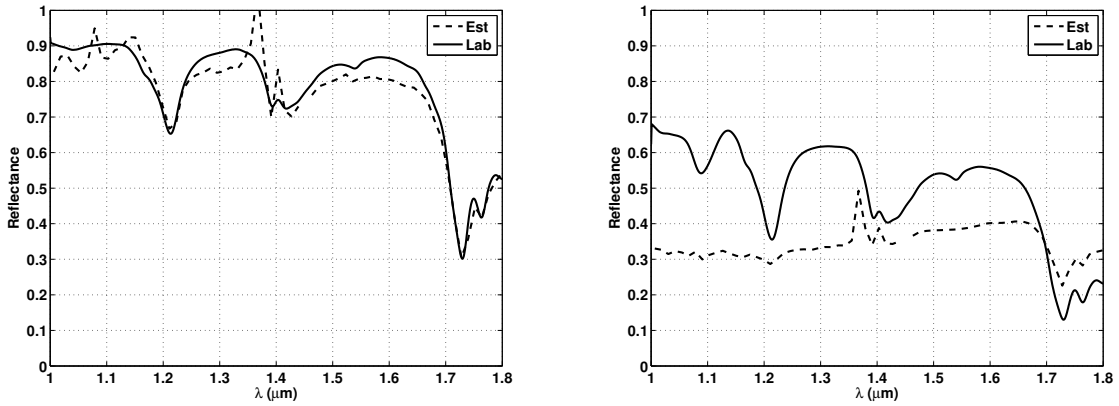

(a) Tyvek **(b) Blue tarp**

Figure 13: Reflectance retrieval using ELM

strates strong agreement with the laboratory measured reflectance. Conversely, the retrieved reflectance of the blue tarp is missing several spectral features near 1.1μm and 1.2μm. These errors may result from geometric bidirectional reflectance distribution function (BRDF) effects that are not explicitly accounted for here. Due to the highly directional nature of laser illumination, BRDF effects may play a more prominent role in HSI exploitation using laser illumination sources.

Turbulence will play an important role in retrieved reflectance as well. To demonstrate the impact of turbulence, reflectance retrieval using ELM is applied to all 1000 temporal measurements for the Tyvek target taken from the brightest pixel (as shown in Figure 12). Figure 14 displays the retrieved reflectances from these measurements along with the temporal standard deviation of the retrieved reflectance as a function of wavelength. Assuming the temporal variability of the sensed radiance is representative of the spatial variability, one would expect significant variability in the retrieved reflectance of the same material. This variability may impact performance for material identificaiton. However, one important observation to note is the turbulence does not appear to change the spectral shape but rather the overall magnitude, which may still allow for spectral identification based upon strong spectral features. Furthermore, a calculation using a simplified turbulence model for the boundary layer predicts that, when sensing from above at airborne altitudes viewing at near nadir geometry, the turbulence noise would be approximately 1/15th of the level from the experiment, and thus comparable to the sensor noise sources. At the experiment geometry, the effect of turbulence increases with range because the beam propagates through the most turbulent atmospheric layer. For a nadir geometry, the turbulence noise is introduced mostly by the bottom layer of the atmosphere (on the order of a few hundred meters) and is essentially independent of altitude.

5. CONCLUSION AND FUTURE WORK

A recently developed 64W breadboard shortwave infrared super-continuum laser was discussed here in the context of use as a potential illumination source for an active HSI system. The laser system was first characterized in

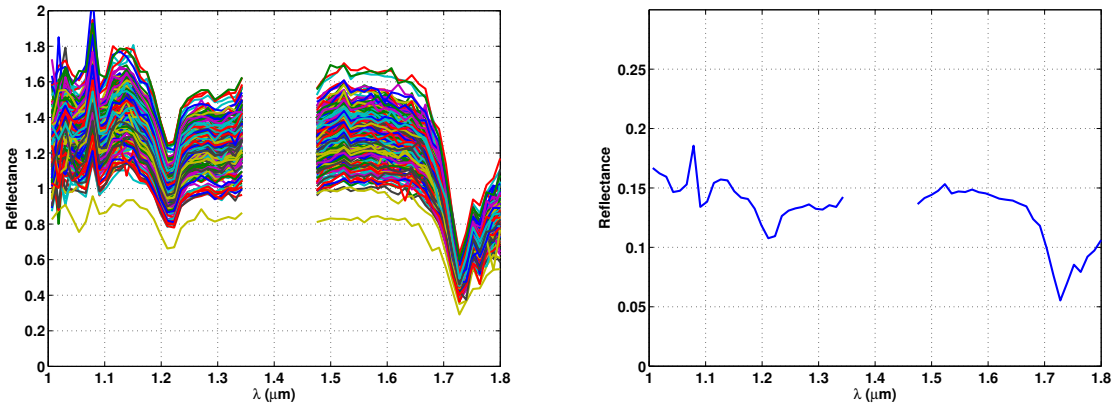

(a) Retrieved reflectance **(b) Standard deviation of retrieved reflectance**

Figure 14: Reflectance retrieval of temporal samples from Tyvek target using ELM to demonstrate atmosperic turbulence effects

the lab to assess the spectral power distribution. Following the lab characterization, a tower test was performed using the laser as an illumination source along a 1.4km slant path onto a target panel. Both broadband and hyperspectral cameras were used to assess laser performance. The results of the tests demonstrate proof-of-concept for use of the laser as an illumination source and for reflectance retrieval of various target materials. The results of the tower test additionally provided insight into the challenges associated with using the SSCL as an illumination source, which include signal degradation due to atmospheric turbulence and potential challenges associated with reflectance retrieval. Omni Sciences, Inc., AFRL, and Leidos are currently collaborating to perform further tower testing using the 64W SSCL to better understand turbulence effects and performance requirements.

REFERENCES

1. B. Stevenson, R. O'Connor, W. Kendall, A. Stocker, W. Schaff, D. Alexa, J. Salvador, M. Eismann, K. Barnard, and J. Kershenstein, "Design and performance of the civil air patrol archer hyperspectral processing system," *Algorithms and Technologies for Multispectral, Hyperspectral, and Ultraspectral Imagery XI* **5806**(1), pp. 731–742, SPIE, 2005.
2. G. Shaw and D. Manolakis, "Signal processing for hyperspectral image exploitation," *Signal Processing Magazine, IEEE* **19**, pp. 12 –16, jan. 2002.
3. M. Eismann, A. Stocker, and N. Nasrabadi, "Automated hyperspectral cueing for civilian search and rescue," *Proceedings of the IEEE* **97**, pp. 1031 –1055, june 2009.
4. D. Manolakis and G. Shaw, "Detection algorithms for hyperspectral imaging applications," *Signal Processing Magazine, IEEE* **19**, pp. 29 –43, jan. 2002.
5. M. T. Eismann, *Hyperspectral Remote Sensing*, SPIE, Bellingham, Washington, 2012.
6. I. Woodhouse, C. Nichol, P. Sinclair, J. Jack, F. Morsdorf, T. Malthus, and G. Patenaude, "A multispectral canopy lidar demonstrator project," *Geoscience and Remote Sensing Letters, IEEE* **8**, pp. 839 –843, sept. 2011.
7. V. V. Alexander, O. P. Kulkarni, M. Kumar, C. Xia, M. N. Islam, F. L. T. Jr., M. J. Welsh, K. Ke, M. J. Freeman, M. Neelakandan, and A. Chan, "Modulation instability initiated high power all-fiber supercontinuum lasers and their applications," *Optical Fiber Technology* **18**(5), pp. 349 – 374, 2012.
8. D. A. Orchard, A. J. Turner, L. Michaille, and K. R. Ridley, "White light lasers for remote sensing," *Technologies for Optical Countermeasures V* **7115**, pp. 711506–711506–8, SPIE, 2008.
9. Omni Sciences, Inc. `http://www.omnisciinc.com/`.

10. V. V. Alexander, Z. Shi, M. N. Islam, K. Ke, M. J. Freeman, A. Ifarraguerri, J. Meola, A. Absi, J. Leonard, J. Zadnik, A. S. Szalkowski, and G. J. Boer, "Power scalable 25w supercontinuum laser from 2 to 2.5um with near-diffraction-limited beam and low output variability," *Opt. Lett.* **38**, pp. 2292–2294, Jul 2013.
11. V. V. Alexander, Z. Shi, M. N. Islam, K. Ke, G. Kalinchenko, M. J. Freeman, A. Ifarraguerri, J. Meola, A. Absi, J. Leonard, J. A. Zadnik, A. S. Szalkowski, and G. J. Boer, "Field trial of active remote sensing using a high-power short-wave infrared supercontinuum laser," *Appl. Opt.* **52**, pp. 6813–6823, Sep 2013.
12. J. Meola, A. Absi, J. D. Leonard, A. I. Ifarraguerri, M. N. Islam, V. V. Alexander, and J. A. Zadnik, "Modeling, development, and testing of a shortwave infrared supercontinuum laser source for use in active hyperspectral imaging," *Proc. SPIE* **8743**, pp. 87431D–87431D–12, 2013.
13. A. Berk *et al.*, "MODTRAN4: Radiative transfer modeling for atmospheric correction," *Proc. SPIE* **3756**, pp. 348 – 353, 1999.
14. A. Berk *et al.*, "MODTRAN4 Version 3 Revision 1 USER'S MANUAL," software manual, Air Force Research Laboratory, Space Vehicles Directorate, Hanscom Air Force Base, 2003.
15. D. C. Dayton and J. B. Lasche, "Estimator of illuminator scintillation in laser illuminated imagery," in *Proc. SPIE*, **8877**, pp. 88770A–1–88770A–8, 2013.